Global Mapping of Structural Solutions Provided by the Extended X-ray Absorption Fine Structure *ab Initio* Code FEFF 6.01: Structure of the Cryogenic Photoproduct of the Myoglobin−Carbon Monoxide Complex[†]

Mark R. Chance,* Lisa M. Miller, Robert F. Fischetti, Eva Scheuring, Wu-Xin Huang, Bianca Sclavi, Yang Hai, and Michael Sullivan

Regional Center for Time-Resolved Synchrotron Spectroscopy, Department of Physiology and Biophysics, Albert Einstein College of Medicine of Yeshiva University, 1300 Morris Park Avenue, Bronx, New York 10461, and National Synchrotron Light Source, Brookhaven National Laboratory, Upton, New York 11973

Received March 6, 1996[⊗]

ABSTRACT: X-ray methods based on synchrotron technology have the promise of providing time-resolved structural data based on the high flux and brightness of the X-ray beams. One of the most closely examined problems in this area of time-resolved structure determination has been the examination of intermediates in ligand binding to myoglobin. Recent crystallographic experiments using synchrotron radiation have identified the protein tertiary and heme structural changes that occur upon photolysis of the myoglobin−carbon monoxide complex at cryogenic temperatures [Schlichting, I., Berendzen, J., Phillips, G., & Sweet, R. (1994) *Nature 371*, 808−812]. However, the precision of protein crystallographic data (∼0.2 Å) is insufficient to provide precise metrical details of the iron−ligand bond lengths. Since bond length changes on this scale can trigger reactivity changes of several orders of magnitude, such detail is critical to a full understanding of metalloprotein structure−function relationships. Extended X-ray absorption fine structure (EXAFS) spectroscopy has the potential for analyzing bond distances to a precision of 0.02 Å but is hampered by its relative insensitivity to the geometry of the backscattering atoms. Thus, it is often unable to provide a unique solution to the structure without ancillary structural information. We have developed a suite of computer programs that incorporate this ancillary structural information and compute the expected experimental spectra for a wide ranging series of Cartesian coordinate sets (global mapping). The programs systematically increment the distance of the metal to various coordinating ligands (along with their associated higher shells). Then, utilizing the *ab initio* EXAFS code FEFF 6.01, simulated spectra are generated and compared to the actual experimental spectra, and the differences are computed. Finally, the results for hundreds of simulations can be displayed (and compared) in a single plot. The power of this approach is demonstrated in the examination of high signal to noise EXAFS data from a photolyzed solution sample of the myoglobin−carbon monoxide complex at 10 K. Evaluation of these data using our global mapping procedures placed the iron to pyrrole nitrogen average distances close to the value for deoxymyoglobin (2.05 ± 0.01 Å), while the distance from iron to the proximal histidine nitrogen is seen to be 2.20 ± 0.04 Å. It is also shown that one cannot uniquely position the CO ligand on the basis of the EXAFS data alone, as a number of reasonable minima (from the perspective of the EXAFS) are observed. This provides a reasonable explanation for the multiplicity of solutions that have been previously reported. The results presented here are seen to be in complete agreement with the crystallographic results of Schlichting et al. (1994) within the respective errors of the two techniques; however, the extended X-ray absorption fine structure data allow the iron−ligand bond lengths to be precisely defined. An examination of the available spectroscopic data, including EXAFS, shows that the crystallographic results of Schlichting et al. (1994) are highly relevant to the physiological solution state and must be taken into account in any attempt to understand the incomplete relaxation process of the heme iron for the Mb*CO photoproduct at low temperature.

Structural information on the *solution* states of biomolecules has been of paramount importance in determining biological function, and *structural spectroscopic* techniques have been instrumental in defining these structure−function relationships for many years. The application of techniques like resonance Raman, FTIR, EPR, NMR, and X-ray spectroscopy to solution samples of biomolecules has revolutionized our understanding of the structure−function relationships controlling biological chemistry. *Time-resolved methods* of structural spectroscopy have been particularly valuable in investigating the dynamics of key structures. A major objective of time-resolved structure−function studies is to gain a better understanding of the structure of intermediate states and thus elucidate the nature of dynamic changes in structure that bridge the static end points provided

[†] This work is supported by NIH Grants HL-45892 and RR-01633. M.R.C. is the holder of the Joseph and Anne Wunsch Fellowship in Biophysical Engineering from the Albert Einstein College of Medicine. L.M.M., R.F.F., E.S., and W.-X.H. contributed equally to this paper. The construction and operation of beamline X9B is supported by the Biotechnology Research Resource program of the National Institutes of Health, P41-RR01633. The NSLS is supported by the Department of Energy, Division of Materials Sciences.

* Author to whom correspondence should be addressed at the Albert Einstein College of Medicine of Yeshiva University. Phone, 718-430-4136; Fax, 718-430-8819; e-mail, mrc@aecom.yu.edu.

[⊗] Abstract published in *Advance ACS Abstracts,* June 15, 1996.

S0006-2960(96)00550-8 CCC: $12.00

by crystallographic or thermodynamic analysis. Crystallographic structural information is not precise enough to characterize small bond lengths changes (<0.2 Å) that are often significant in regulating protein reactivity. In this paper, we provide a logical extension to the prior uses of theoretical multiple scattering codes wherein EXAFS[1] experimental data can be compared to a series of potential structural solutions. The advantage afforded by the programs we have developed is that a number of potential solutions are simultaneously compared in an even-handed fashion, and both the errors intrinsic to the fit and potential multiple minima can be easily visualized.

The biological process of interest is ligand binding to myoglobin, which has been intensely studied by the biophysics community. This is due, in part, to its intrinsic interest as a carrier of oxygen in the heart muscle (Wittenberg & Wittenberg, 1989) as well as its role as a model protein for examining both the chemistry of heme proteins (Chance, 1986; Springer et al., 1994) and theories of protein dynamics in general (Austin et al., 1987; Frauenfelder & Wolynes, 1985; Srajer et al., 1986). The binding of ligands to myoglobin involves both an outer barrier, where the ligand must traverse the protein matrix, and an inner barrier at the heme. Below 160 K the ligand cannot escape from the protein matrix (Austin et al., 1975), so the rebinding reaction can be characterized by the following:

$$\underset{A_i}{MbCO} \overset{h\nu}{\longleftrightarrow} \underset{B_j}{Mb^*CO}$$

Photolysis effects a conversion from A states (ligand on) to B states (ligand off), with the ligand trapped in the vicinity of the heme. Elapsed time or increases in temperature lead to rebinding of the ligand with the heme and thus, reformation of A states. Below 20 K, when the ligand is carbon monoxide (CO), 100% conversion to B states is achieved with little rebinding (Alben et al., 1982; Iizuka et al., 1974). The A states (different conformations of liganded MbCO) are characterized by the infrared stretching frequency of the bound CO ligand as it is sensitive to the CO bond strength. These frequencies are observed in the range of 1920−1970 cm^{-1} (Caughey et al., 1981; Makinen et al., 1979). The rates of interconversion between the different A states at temperatures below 160 K are so low that interconversions between the A states are not observed as a result of photolysis and recombination cycles (Ansari et al., 1987; Chance et al., 1987). The B states, generated by photolysis of the myoglobin−carbon monoxide complex (MbCO), also have (weak) infrared signatures seen from 2120 to 2140 cm^{-1} (Alben et al., 1982). The variation in infrared properties of the different A and B states are assumed to arise from distinct interactions of the CO ligand with the distal heme pocket residues. In fact, site-directed mutagenesis of the His E7 and Val E11 residues provides considerable alteration in infrared properties of both A and B states, and these alterations are reasonably correlated with changes in the polarity of the heme pocket (Braunstein et al., 1993; Quillin et al., 1995; Ray et al., 1994; Springer et al., 1994).

Understanding the structure of B states using a variety of spectroscopic techniques has been of long-standing interest (Chance, 1993), since these states represent a potential way station for the ligand along its functional trajectory, essentially providing a frozen snapshot of the reaction between the well-established end points. The visualization of this snapshot became a reality with the recent crystallographic determination of the MbCO photoproduct (Mb*CO) at 20 K to 1.5 Å resolution (Schlichting et al., 1994). The exciting features of this structure were (1) the ligand was located in the heme pocket 3−4 Å from the iron atom essentially parallel to the heme and (2) the proximal histidine−iron coordinate had moved close the deoxy structure but was essentially relaxed only 75% toward the deoxy coordinates. This provided reasonable structural interpretations for both the infrared signature of the B states, which are close to the free gas value of the CO stretching frequency (Alben et al., 1982; Ansari et al., 1987), and the high-spin ($S = 2$), out-of-plane spectroscopic assignment for the iron atom based on optical, Mossbauer, magnetic susceptibility, and X-ray absorption spectroscopy (XAS) data (Chance, 1993; Iizuka et al., 1974; Marcolin et al., 1979; Miller & Chance, 1995; Roder et al., 1984; Spartalian et al., 1976). In addition, recent time-resolved photoselection spectroscopy experiments have provided additional details about the CO ligand geometry in the bound state and its trajectory upon photolysis (Lim et al., 1995).

Multiple scattering EXAFS codes have been developed to evaluate the complex scattering interactions of natural ligands in metalloproteins. The relevant applications have steadily grown, from simulations of scattering groups like simple histidines to complex porphyrin macrocycles (Blackburn et al., 1988; Co & Hodgson, 1981; Hasnain & Strange, 1990; Knowles et al., 1989; Liu et al., 1994; Mustre de Leon et al., 1991; Nordlander et al., 1993; Rehr & Albers, 1990; Rehr et al., 1991, 1992; Strange et al., 1987; Westre et al., 1994). We chose to utilize the FEFF program version 6.01, which has had considerable testing and success relative to known structures (O'Day et al., 1994). The development of refinement techniques coupled to multiple scattering codes (Binstead et al., 1992), where crystal structure data (generally from a database of small molecule data) are explicitly utilized to reduce the number of degrees of freedom in the structure, allows the entire EXAFS spectrum as opposed to Fourier-filtered shells to be analyzed to provide a solution. This technique is also frequently utilized to refine protein crystal structure data (Brunger, 1987). Such refinement procedures differ from multiple scattering based fitting procedures, where models are generated using the multiple scattering formalisms and then used in nonlinear least squares fitting procedures to provide the "best fit" to the experimental data. However, both methods provide excellent simulations of the unfiltered EXAFS data in the range of the wave vector (k, $Å^{-1}$) from 4 and higher.

We have further explored constrained refinement (Binstead, 1992), focusing on global mapping where a grid of hundreds of simulations are directly compared to the experimental data with minimal use of nonlinear least squares fitting procedures to find the interatomic distances. Each simulation is performed with different interatomic distances.

[1] Abbreviations: CO, carbon monoxide; EXAFS, extended X-ray absorption fine structure; MbCO, myoglobin−carbon monoxide complex; Mb*CO, photolyzed myoglobin−carbon monoxide complex; N_e, proximal histidine nitrogen; N_p, pyrrole nitrogen; XAS, X-ray absorption spectroscopy.

The advent of fast, inexpensive Pentium and Power PC computers makes such calculations within the reach of any laboratory. The emphasis of our approach is to map the local and global minima and provide a detailed visual picture and error analysis in the comparison of alternative structures. The three-dimensional structural coordinates utilized in the simulations are based on crystal structure models derived from structural databases. Thus, a particular geometry for the metal site is incorporated in this choice. Alternative structures with different geometries can also be selected, processed, and compared. This makes the structural assumptions about the site explicit, and they must be justified on the basis of ancillary structural information. Our suite of programs (called AUTOFIT 1.0) start with the selected structure file, vary selected bond distances, compare the resulting *ab initio* simulations to the experimental data, and compute and plot a figure that displays 400−500 alternative solutions simultaneously. We settled on a pseudo-three-dimensional representation wherein *x* and *y* values represent particular bond distances that are varied (for example, iron−histidine nitrogen and iron−pyrrole nitrogen distances), while the color of the intersecting squares indicates the adequacy of the fit. Yellow indicates the best fit of the grid, ranging to red, blue, green, and black.

Several previous EXAFS investigations (Chance et al., 1983; Powers et al., 1987; Teng et al., 1987) have provided conflicting values for the iron−pyrrole nitrogen distances and the distance to CO in the heme pocket. We utilized global mapping methods to investigate the possible reasons for the variations in observed solutions. We also collected new experimental data that are extremely high in signal−noise so that the fitting can be carried over a *k* range of 4−15 $Å^{-1}$. In addition, the intermediate state has been verified with respect to sample occupancy by low-temperature optical spectroscopy before and after EXAFS data collection. The results presented here demonstrate that the EXAFS spectra can accurately determine a number of important structural parameters for heme proteins; however, the presence of multiple minima invites caution in the structural interpretations.

METHODS

Sample Occupancy. Horse skeletal muscle myoglobin was purchased from Sigma. MbCO was prepared at 0.5 mM concentration, and the sample was adjusted to pH 9.0 with 100 mM potassium phosphate buffer as described previously (Miller & Chance, 1994, 1995). We have recently shown that, at low temperature, horse skeletal muscle myoglobin exhibits a single A state at pH 9.0 [A_1, 1946 cm^{-1} (Miller & Chance, 1995)] and a single B state subsequent to photolysis (unpublished observation). Thus, we consider it preferable for these investigations. It should be noted that each previous determination of the B-state structure may have inadvertently utilized a different population of substates. The crystallographic result (recombinant sperm whale) is likely based on an A_0 substate (Zhu et al., 1992). The EXAFS investigations of Powers et al. (1987) used sperm whale MbCO at pH 6.4, which has a mixture of A_1 and A_0 states, while those of Teng et al. (1987), which utilized a dried MbCO film, were also likely based on the A_0 substate (Brown et al., 1983). The different A states give rise to different B states, and the effect of this on the results of these different investigations is of significant interest. Optical and infrared characterizations of the low-temperature photoproduct states were carried out as described previously (Miller & Chance, 1994, 1995) and are briefly repeated here. The sample (0.5 mM, 0.5 mm thickness) was mounted in a low-temperature cryostat (Janis ST-4B) which was interfaced to a Lakeshore temperature controller (Model 805). Samples were cooled via a liquid helium transfer line. The cryostat was fitted with mylar windows to allow the X-ray beam to pass while still maintaining vacuum for the cryogenic cooling. Optical spectra were taken using a Hewlett Packard diode array spectrometer (Model HP8452A). The data collection time was 0.1 s for each spectrum to prevent photolysis of the sample by the spectrometer's deuterium source lamp. A reference spectrum of air was taken; then a spectrum of the MbCO sample at 8 K in the cryostat was taken. This is shown in Figure 1. The sample was then photolyzed for 5 min on each side using a high-intensity white light source (CUDA Products, Inc., Model I-150). Another spectrum was recorded. The photoproduct spectrum (Mb*CO) is also shown in Figure 1. This spectrum is equivalent to a deoxymyoglobin spectrum taken under the same conditions and is consistent with 95−100% photolysis (Chance et al., 1990; Miller & Chance, 1995). The cryostat could be moved easily from the UV−vis spectrometer to its aligned location in the X-ray beam while maintaining cryogenic conditions. These procedures assured that the X-ray measurements were carried out on well-characterized samples.

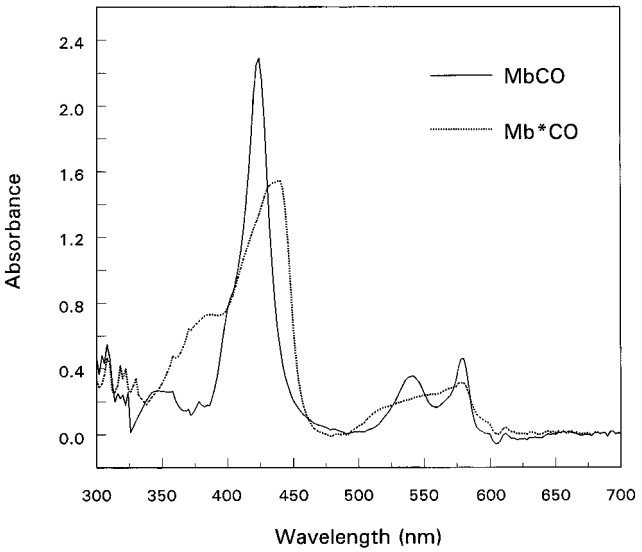

FIGURE 1: On-line optical monitoring of EXAFS sample. The spectra of the sample before and after photolysis are shown. The data collection time was 0.1 s for each spectrum to prevent photolysis of the sample by the spectrometer's deuterium source lamp. A reference spectrum of air was taken; then a spectrum of the MbCO sample at 8 K in the cryostat was taken (solid line). The sample was then photolyzed for 5 min per side using a high-intensity white light source. A spectrum of Mb*CO was recorded (dotted line). This spectrum is equivalent to a deoxymyoglobin spectrum taken under the same conditions and is consistent with 95−100% photolysis (Chance et al., 1990; Miller & Chance, 1995).

Dynamical Focusing Monochromator. Maximizing the signal to noise of X-ray spectroscopic data requires maximizing the effective count rate (Warburton, 1986):

$$N_{\text{eff}} = (N_A + N_B)^2/(N_B) \quad (1)$$

where N_A is the number of counts above the X-ray edge and

N_B is the number of counts below the edge. This formula explicitly acknowledges the degradation of the XAS spectroscopy signal caused by increasing backgrounds. The development of energy-resolving detectors as common place tools has reduced N_B considerably for typical experiments; however, the count rate limitations of the detectors limit the N_A values that are attainable (Cramer et al., 1988; Warburton, 1986). Due to the need to assure adequate photolysis and optical monitoring of the myoglobin sample, we settled on a concentration of 0.5 mM. At metal concentrations less than 1 mM the ratio of signal to background needs to be improved for high signal to noise data to be acquired. To increase the available X-ray flux to optimize these experiments, hardware modifications were made to the X-ray spectroscopy beamline X-9B at NSLS.

The monochromator on beamline X-9B at the National Synchrotron Light Source is a double crystal design. Horizontal focusing can be achieved by replacing the flat, second crystal with a thin crystal which is mounted in a bending stage and is elastically bent to a cylindrical or conical cross section (Habenschuss et al., 1988). The crystal has steel ribs (0.6 mm thick) glued to the back side of the crystal at a spacing of 3 mm in order to reduce the effect of anticlastic bending (Sparks et al., 1982). The Si(111) crystal is 65 mm wide and can collect up to 3.9 mrad of synchrotron radiation in the horizontal direction. The horizontal focal size ranges from 0.3 to 0.7 mm full width at half-maximum. The smallest focal sizes are observed at the highest X-ray energies and shortest monochromator to focus distances (focal lengths). The current X-ray energy range for the sagittal focusing monochromator is 4.0−11.9 keV. An 800 mm long nickel mirror collects all of the vertical divergence from the source and can provide vertical focusing when elastically bent to an elliptical cross section. However, for these experiments the mirror was flat and held at an angle of 4.5 mrad to reject higher harmonics. The measured X-ray flux at the beamline with the sagittal monochromator installed, primary apertures (X-ray beam defining slits before the optics) and the hutch apertures (X-ray beam defining slits after the optics) fully open, and the mirror set at an angle to provide harmonic rejection is in the range of $1.8-3.1 \times 10^{11}$ photons s^{-1} per 100 mA of beam current per 3.9 mrad of horizontal acceptance per 0.1% bandwidth for 6−11 keV. The experiments of this paper were carried out with vertical slits set at 1.5 mm and approximately 2×10^{11} photons s^{-1} of beam flux. This is four times the flux delivered to the specimen over the alternative flat crystal monochromator (for a typical sample size of 15 mm width).

For these spectroscopic experiments, since the sample was 6 mm in diameter, only a 1 mm focus was maintained on the sample. The sample was mounted at the usual 45° incidence, and the germanium detector viewed the sample at 90° relative to the incident X-ray beam. A calibration channel with an iron foil was also utilized to account for any energy shifts in the monochromator. Due to the high flux, incident count rates on the detector were high enough to cause dead time losses that were significant (Cramer et al., 1988). The detector incident count rate was reduced to 40 000 counts s^{-1} $channel^{-1}$ by placing a vacuum flight tube in front of the cryostat and guard slits in front of the sample. In addition, the detector was carefully shielded with lead. The small, well-defined beam and a detection geometry close to ideal (90°) for all channels of the 13-element detector improved the N_{eff}. The N_{eff} for the experiments was increased 3−4-fold relative to the running conditions with the flat crystal monochromator.

Sixteen EXAFS scans of the Mb*CO photoproduct sample were collected on four separate samples. The pre-edge, edge, and near-edge data were acquired as described previously (Chance, 1986; Miller & Chance, 1995). The EXAFS data were collected in equally spaced points in k space separated by 0.05 $Å^{-1}$ from $k = 2.0$ to $k = 15.0$. The signal averaging was weighted linearly in k, so that 2 s per point was used at $k = 2$ and 15 s per point was used at $k = 15$. Each scan lasted about 45 min. The k^3-weighted and background-subtracted data are shown in Figure 2 (ten of the best scans were coadded).

FEFF Simulations, Structural Refinements, and Error Analysis. FEFF 6.01 was licensed from the University of Washington. Structures were examined using the CHEMX molecular modeling program (CHEMX is developed and designed by Chemical Design Ltd., Oxford, England) on a Silicon Graphics Indigo computer. The structural coordinates for Mb*CO were kindly provided by Dr. Joel Berendzen; refinements were final for the atoms within 5 Å of the heme. The Mb*CO crystal structure formed the basis for the FEFF EXAFS simulations that were used at each point of the grid. This is the key starting point for our suite of programs (AUTOFIT 1.0). The Mb*CO structure file contains the Cartesian coordinates of all the atoms [with the central metal in the (0,0,0) position] as well as the appropriate connectivity information. This file is limited to those atoms at a distance of 5 Å or less from the central metal, since these are the only atoms that provide a significant EXAFS backscattering signal. In this case, we used the Mb*CO coordinates for the structure file; however, a number of alternatives could have been employed. This structure file explicitly incorporates the geometric assumptions about the site, for example, the iron displacement and histidine tilt and orientation. Thus, for EXAFS problems where the geometry is not known, several structure files would be selected for evaluation that encompass the set of reasonable assumptions and each would be examined separately.

The programs move particular iron ligands and their associated higher shells as structural units under user control. Particular atoms and the structural units associated with them are varied while all other atoms are left unaltered. Once the structural coordinates have been calculated, an appropriate FEFF input file is generated. Further details of the programs will be presented elsewhere; copies of the program are available from the corresponding author. In short, the program automatically generates a series of structures and their *ab initio* simulations. These are then compared to the experimental EXAFS data on the basis of information provided in a series of parameter files that appear to the user as menus. The output is saved and converted to plotted formats as seen in Figures 4 and 6−8.

The FEFF 6.01 simulations were carried out on Gateway P5-60 or P5-90 computer systems, with the following flags enabled. Core hole 1 = K edge; S_0^2 (amplitude reduction factor) = 0.85; $R_{max} = 5$ Å; NLEG = 5 (up to five scattering paths with total distances ≤5 Å were evaluated). The Debye−Waller factors were set to zero for the FEFF simulations. Unique potentials were assigned to Fe, N, O, and C atoms. Further details of the simulations are discussed

in Results and Discussion. Data processing, where specified, was carried out using a PC-based Bell Labs EXAFS package compiled with Microsoft FORTRAN 77 (Rowlett et al., 1994; Scheuring et al., 1994). For Figures 4 and 6−8 the experimental data and the simulations were k^3 weighted, Fourier transformed, filtered from 0.8 to 4.8 Å, back-transformed, and processed by using the Bell Labs EXAFS package. All evaluations of $\sum R^2$ were carried out in the range of 4−15 Å^{-1}. A series of 400 simulations takes 10−12 h of computation on the Pentium PCs.

The EXAFS data resulting from the FEFF simulations are k^3 weighted, compared to the experimental data, and the sum of residuals squared is calculated:

$$\sum R^2 = \sum_i \{(k^3\mathrm{X}_i)_{\text{experimental}} - (k^3\mathrm{X}_i)_{\text{simulation}}\}^2 \quad (2)$$

In cases where particular shells are emphasized, and the data is Fourier filtered, identical data ranges and filter windows were utilized for the FEFF simulation and the experimental data. For each grid position the $\sum R^2$ is minimized with respect to ΔE_0 and $\Delta\sigma^2$ values in a one atom type refinement to assure that a stable solution is obtained; the values were permitted to vary up to 10 eV and 0.01 Å^2, respectively (Chance, 1986; Chance et al., 1992; Lee et al., 1981; Rowlett et al., 1994). In practice, the maximum values observed for these parameters were typically half these limits for the simulations reported here. Thus, the Bell Labs package was essentially used mainly to process data with equivalent k grids and to compute sum of residuals squared.

Figure 3a shows the structural coordinates for the Mb*CO photoproduct after cutting out all atoms further than 5 Å from the iron atom. Notice that this excludes the vinyl and other peripheral groups of the heme, and it includes only the imidazole parts of the proximal histidine, the nitrogen from the distal histidine (His E7), and a carbon atom from valine (Val E11). Thirty-four atoms overall are included in the simulation of this structure. Figure 3b outlines software steps that automatically calculate the grid with user-defined ranges and increments.

Error analysis is carried out by a variation of the methods outlined by Lytle et al. (1989) and further developed in depth by Powers and Kincaid (1989). The number of degrees of freedom of EXAFS data, N_{df}, is calculated as follows (Lee et al., 1981; Powers & Kincaid, 1989):

$$N_{\text{df}} = (2 \times \Delta r \times \Delta k)/\pi \quad (3)$$

Thus, for a Δr of 4 Å and a k range from 4 to 15 Å^{-1} the refinement of nearly 30 independent parameters can be supported. For Fourier-filtered data, the number of free parameters in the fit (N_{ff}) is simply the number of degrees of freedom (N_{df}) in the filtered data minus the number of parameters (N_{p}) in the fitting procedure:

$$N_{\text{ff}} = N_{\text{df}} - N_{\text{p}} \quad (4)$$

The error for a particular parameter (of particular interest are the bond distances) can be evaluated by examining the systematic variation of that parameter with respect to the behavior of the sum of residuals squared ($\sum R^2$) around the minimum value such that when $\sum R^2$ increases by a factor of $[1 + (1/N_{\text{ff}})]$, the error limit has been reached. This equation adjusts the error limits appropriately if the N_{ff} value is high (due to an excess of free parameters in the filtered data relative to the number of parameters in the fit) so that small changes in ΣR^2 become significant. We have modified the equation so that when the sum of residuals squared increases to

$$\sum R^2_{\text{minimum}} \times [1 + (N_{\text{p}}/N_{\text{df}})] \quad (5)$$

the error limit is reached. The number of degrees of freedom are 28 for Figures 4 and 6−8. There are two distances varied on each grid, and each intersection point is minimized with respect to E_0 and $\Delta\sigma_2$; thus the effective number of refinable parameters (N_{p}) is 4, and the error limit is reached when $\sum R_2$ increases 15% above the minimum value for Figures 4 and 6−8. In practical terms this means errors in the iron−pyrrole nitrogen average distance of ±0.01 Å and errors in the iron−histidine nitrogen distance of ±0.04 Å, which are reasonable on the basis of previous analysis and the signal to noise of the data (Chance, 1986; Powers et al., 1987).

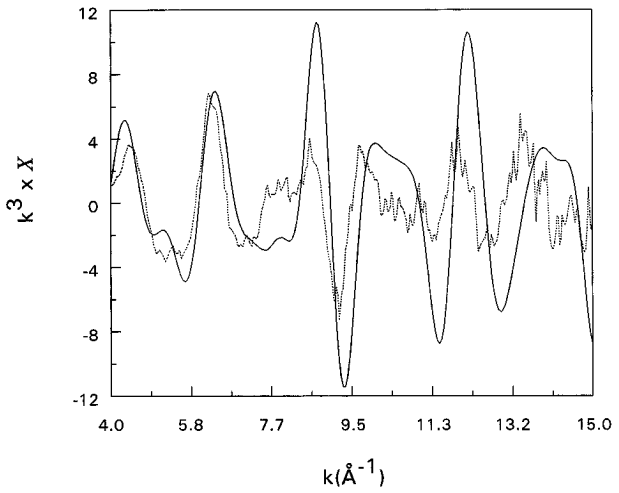

FIGURE 2: k^3-weighted, background-subtracted raw experimental data for Mb*CO (dotted line) compared to FEFF simulation using the crystallographic coordinates of Schlichting et al. (1994) (solid line). A cursory examination shows a mismatch in the phase relationships; in addition, the amplitude of the simulation is 2 times too large.

RESULTS AND DISCUSSION

*Global Mapping of the Mb*CO Structure by EXAFS.* The EXAFS spectrum predicted from the crystallographic coordinates for the Mb*CO photoproduct was calculated and is compared to the experimentally collected data in Figure 2. A cursory examination shows a mismatch in the phase relationships, with the experimental data exhibiting a higher overall frequency than the simulation, implying that the crystallographic coordinates have an overall average of the interatomic distances that is too short to adequately model the data. In addition, the amplitude of the simulation is nearly 2 times too large. A longer average distance from iron to the pyrrole rings would be predicted to reduce the amplitude of the simulation and increase the frequency, allowing a better match to the experimental data. In order to refine the structure to better model the EXAFS data, the positions of atoms were varied in a systematic fashion. Figure 3a shows the original structure as provided by crystallography and the atoms that are included in the simulation. The calculation of the global grid was carried out according to the overall procedure outlined in Figure 3b. The FEFF program calculates scattering paths for photo-

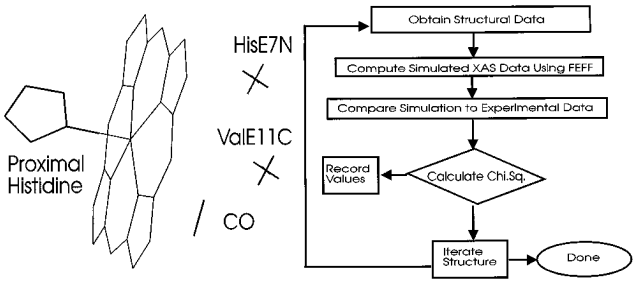

FIGURE 3: (a, left) The original structure as provided by crystallography and all the atoms that are included in the simulation are shown. This view was created by deleting all atoms outside a sphere defined by a radial distance 5 Å from iron. The ejected photoelectron in an EXAFS experiment has a mean free path that precludes observing atoms further removed from the central absorber. (b, right) This scheme shows the overall simulation procedure.

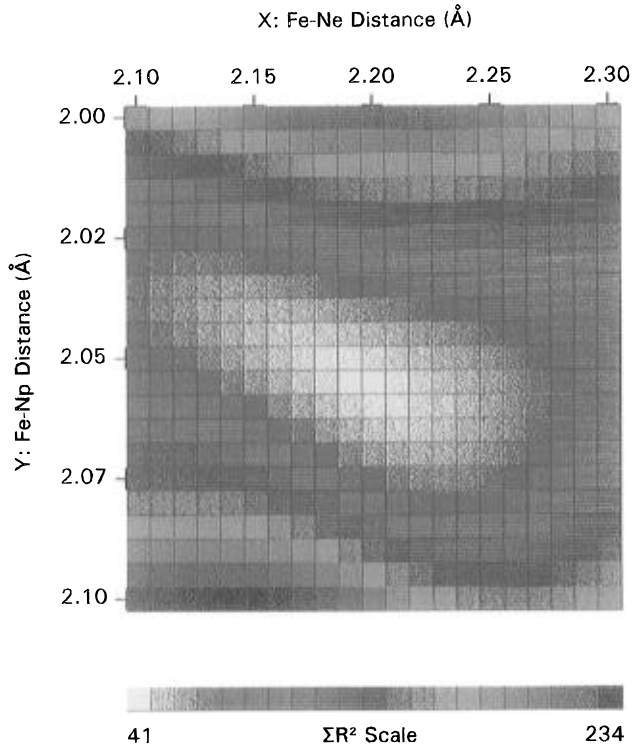

FIGURE 4: Simulation grid for the Fe−histidine and Fe−pyrrole nitrogen distances with increments for the Fe−histidine distance of 0.01 Å and increments for the pyrrole nitrogen distances of 0.005 Å. The Fe−CO distance was held fixed at the crystallographic distance. Simulations that are statistically valid are predominantly yellow in color; when substantial red shading is seen, $\sum R^2$ increases 15% or more above the minimum, and the error limit is reached. Thus, the error in the Fe−histidine distance is ±0.04 Å while the error in the iron−pyrrole nitrogen average distance is ±0.01 Å.

electron ejections that involve single and multiple scattering paths of <5 Å. The amplitude and phase for each path is calculated. In order to simulate the EXAFS spectrum from the structural coordinates for every point on the grid, nearly 200 scattering paths were examined and calculated; paths that had curved wave amplitudes at less than 3% of the major contributor were discarded.

The simulations of Figure 4 represent a grid where the iron−histidine distance was varied from 2.10 to 2.30 Å in 0.01 Å increments while the four iron−pyrrole nitrogen distances were varied as a unit from 2.00 to 2.10 Å in increments of 0.005 Å. A sharp, well-defined minimum is observed at an iron−pyrrole nitrogen distance of 2.05 ± 0.01 Å and a histidine distance of 2.20 ± 0.04 Å. These results are in agreement with the crystallographic results, even if the crystallographic errors are assumed to be as small as ±0.1 Å, which is unlikely. The comparison of the FEFF simulation of the minimum solution to the k^3-weighted experimental data is shown in Figure 5. This is a distinct improvement over Figure 2 and represents a very good fit for a data range of 4−15 Å^{-1}. It should be clearly noted that these structural results were obtained with virtually no fitting at all. Only Debye−Waller and E_0 parameters were refined in a one atom type procedure to yield indicated fit. Thus, we are using a *minimum* of free parameters to fit the data. We could provide a smaller $\sum R^2$ and an even better match to the experimental data using the traditional method of fitting individual Fourier-filtered contributions (or the unfiltered EXAFS spectrum) with a series of models that explicitly include the multiple scattering and with multiple fitting parameters for each shell. The advantage of the grid-mapping technique is that we can explicitly compare different structural solutions in an even-handed manner with far fewer fitting parameters.

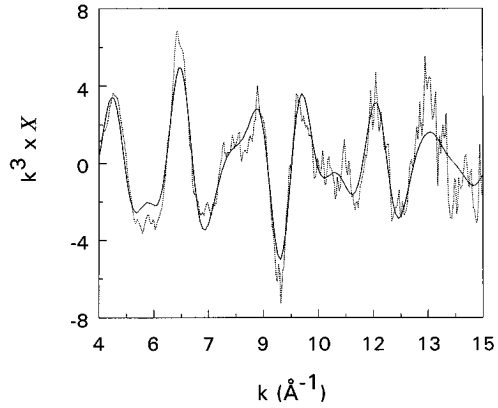

FIGURE 5: k^3-weighted, background-subtracted raw experimental data for Mb*CO (dotted line) compared to FEFF simulation (solid line) using the coordinates suggested by the minimum in Figure 4.

In Figure 6, we expand the grid (outlined in Figure 4) to include a much wider range of simulated distances, including distances that are outside the range of crystallographic error. Thus, the iron−pyrrole nitrogen distance is varied from 1.95 to 2.15 Å in increments of 0.01 Å and the iron−histidine distance from 1.75 to 2.70 Å in increments of 0.05 Å. Figure 6 shows two clear local minima and a third fainter minimum. Each of these minima can be seen as a diagonal feature extending from the upper left to the lower right, all centered at iron−pyrrole nitrogen distances of 2.03−2.05 Å and at iron−histidine distances of 1.90, 2.20, and 2.50 Å.

What is the source of these alternative solutions and which of them represent the correct iron−histidine distance? Based on $\sum R^2$ alone, the minimum centered at an iron−histidine distance of 1.90 Å can be ruled out since the $\sum R^2$ value is 40% higher than the global minimum, where the error limits are at $\sum R^2$ values 15% higher than the minimum. However, the minimum centered at an iron−histidine distance of 2.50 Å has an $\sum R^2$ value that is only 10% higher than the global minimum; thus it cannot be excluded on this basis. However, this value of 2.50 Å is 0.25 Å longer than the crystallographic value and implies a *very* weak iron−histidine bond, inconsistent with Raman data (see below). This pattern of multiple minima for the iron−histidine distance is a consequence of the distance dependence of the phase of the sinusoidal EXAFS oscillations. The frequency of the oscillations is

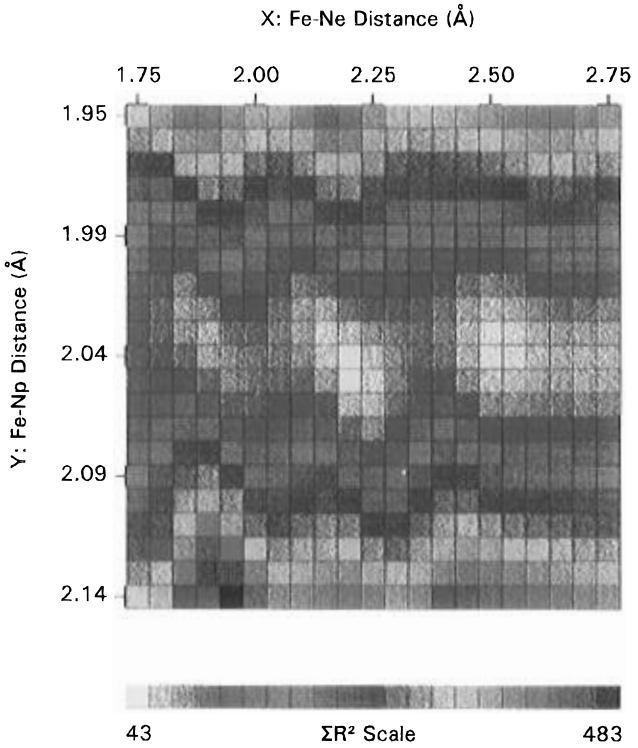

FIGURE 6: Simulation grid for the Fe−histidine and Fe−pyrrole nitrogen distances with increments for the Fe−histidine distance of 0.05 Å and increments for the pyrrole nitrogen distances of 0.01 Å. Three minima are seen; the best minimum is the one seen in Figure 4; however, the difference in $\sum R^2$ between this minimum and the one centered at a longer histidine distance is statistically insignificant. The latter is ruled out on the basis of the crystallographic and Raman data.

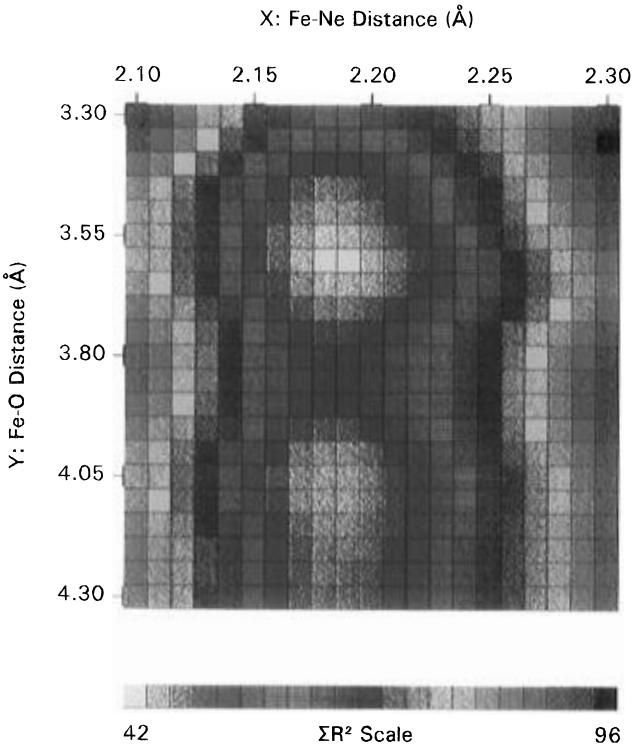

FIGURE 7: Simulation grid for the Fe−histidine and Fe−CO distances with increments for the Fe−histidine distance of 0.01 Å and increments for the iron−CO distance of 0.05 Å. Two minima are found; the one with the CO ligand further from iron is not ruled out by the statistics.

2*kr*, and these distance solutions represent "multiples" of a fundamental oscillation that come "in phase" periodically (about every 0.3 Å). Such "multiple minima" are often encountered when analyzing Fourier-filtered data (Lee et al., 1981). However, such multiple minima have never been shown for the fitting of heme protein spectra.

We also analyzed the effect of moving the CO ligand on the simulations. These results are shown in Figure 7, where the CO distance is varied beyond the range of the crystallographic error for the CO distance and where the histidine is varied in a relatively narrow range. A clear minimum is found at a distance of 3.6 Å, identical to the crystallographic value. A second minimum is seen at a distance of 4.1 Å with an $\sum R^2$ value 10% higher than that of the alternative minimum, while an increase of at least 15% would be required to rule the minimum out. The CO ligand observed in the heme pocket by crystallography has one atom at 3.6 Å and the second atom at 4.1 Å. Thus, the minimum at the longer distance is likely due to the backscattering signal from the second atom. It should be noted that both methods are insensitive to whether the O or the C ligand is closer to the heme. However, this result indicates that assigning a unique position for the CO ligand by EXAFS alone is difficult.

In order to evaluate other possible solutions, including those that have been suggested by previous investigators, we performed simulations that span a greater range of bond distances (Figure 8). A number of different solutions are seen, although none provide fits better than the minimum congruent with the crystallography data. It is likely that the CO backscattering signal is too small compared to the noise of the data to have its position uniquely defined by EXAFS

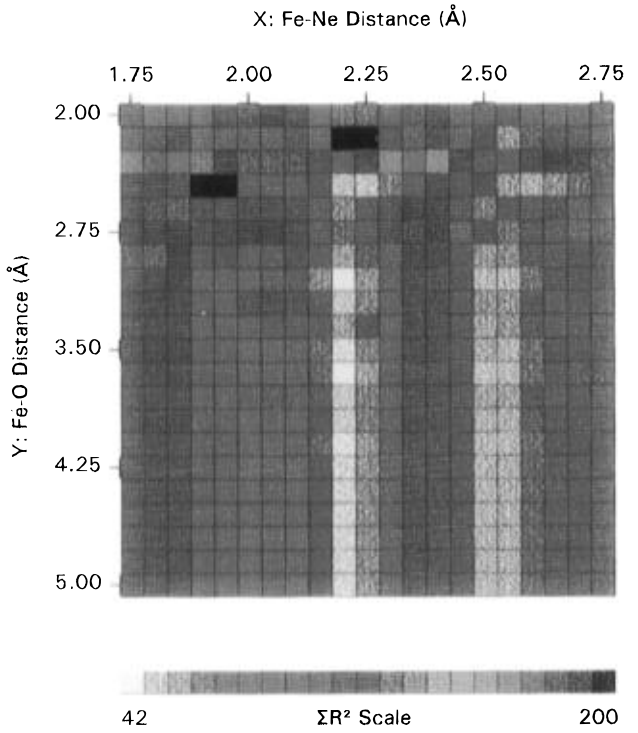

FIGURE 8: Simulation grid for the Fe−histidine and Fe−CO distances with increments for the Fe−histidine distance of 0.05 Å and increments for the iron−CO distance of 0.15 Å. Several statistically valid minima are observed along the grid line where the Fe−histidine nitrogen distance is 2.20 Å. The two best solutions are at the crystallographic position of Schlichting et al. and 0.6 Å shorter.

alone. Examination of the individual FEFF scattering paths shows that the total CO signal is only 6% of the amplitude

Table 1: XAS and Crystal Structure Parameters[a] for Mb*CO by Various Investigators

complex	Fe−N_e (Å)	Fe−N_p (Å)	Fe−CO (Å)	Fe−C_t (Å)
4 K Mb*CO XAS[b]	2.22	2.03	1.97	0.27
40 K Mb*CO XAS[c]	2.20	2.045	2.58	ND[k]
5 K Mb*CO XAS[d]	2.19	1.97	2.3	ND
10 K Mb*CO XAS[e]	2.20 ± 0.04	2.05 ± 0.01	3.6 ± 0.05[j]	0.27[h]
40 K Mb*CO crystal data[f]	2.11 ± 0.1	1.98 ± 0.1	2.7	0.1
20 K Mb*CO crystal data[g]	2.25 ± 0.1	1.98 ± 0.1	3.6 ± 0.1	0.27
deoxy-Mb−XAS[c,d]	2.05−2.1 ± 0.05	2.06 ± 0.02	∞	0.35[h,i]

[a] Fe−N_e = iron−histidine nitrogen distance; Fe−N_p = iron−pyrrole nitrogen average distance; Fe−CO = distance from iron to the carbon of CO; Fe−C_t is the iron out of heme plane displacement. [b] Chance et al. (1983). [c] Powers et al. (1987). [d] Teng et al. (1987). [e] This work. [f] Teng et al. (1994). [g] Schlichting et al. (1994). [h] Miller and Chance (1995). [i] Srajer et al. (1988). [j] Multiple minima are seen for this parameter based on the XAS data alone; see Figures 7 and 8 and text. [k] ND is not determined.

Table 2: Summary of Resonance Raman and Near-IR Frequencies (cm^{-1}) of Myoglobin Complexes

complex	ν_2	ν_4	ν_{Fe-His}	band III
deoxy-Mb	1563[a]	1353[a]	227[a]	13149[b]
Mb*CO	1560[a]	1352[a]	233[a]	13063[b]
MbCO	1590[a]	1375[a]	none	none

[a] Powers et al. (1987); Rousseau and Friedman (1988). [b] Chance (1993).

of the single scattering pyrrole nitrogen signals (when it is at the crystallographic distance). The many atoms of the pyrrole ring provide conflicting signals to make the placement of the CO ligand by the EXAFS alone problematical.

*Spectroscopic Characterization of Mb*CO.* In Table 1, the numerous attempts to accurately define the structure of the Mb*CO intermediate are summarized. This structural data must be put in the context of the available spectroscopic information on Mb*CO, as well as its ability to explain the reactivity (e.g., rebinding rate) of the species. The first successful attempt to characterize Mb*CO was made by Yonetani and co-workers over 20 years ago (Iizuka et al., 1974). They utilized the near-infrared region of the spectrum to search for a deoxy-like band of the Mb*CO photoproduct. Their success led to close examination of this absorption band, which was assigned as a porphyrin $a_2u(\pi) \rightarrow$ iron d_{yz} transition (Eaton et al., 1978; Makinen & Churg, 1982). Thus, it was deemed sensitive to iron displacement, and the general conclusion was that Mb*CO was "deoxy-like" in its structure, although this could not be accurately quantitated. Mossbauer results confirmed the high-spin, $S = 2$ nature of Mb*CO (Spartalian et al., 1976), and this in conjunction with known crystallographic results on model compounds supported a structure near that of deoxy model hemes, which had iron substantially out of the plane and an expanded heme core with elongated Fe−N_p distances [reviewed in Jameson and Ibers (1994)].

Concurrent development of resonance Raman spectroscopy, which examined a number of heme proteins and their model compounds (Spiro & Burke, 1976; Spiro et al., 1979; Spiro & Strekas, 1974; Stong et al., 1980), was followed by examination of the Mb*CO state (Powers et al., 1987; Rousseau & Friedman, 1988). Table 2 shows several experimental results of significance. First, ν_2, the "core-size" marker, is slightly broader for Mb*CO and shifted 2−3 cm^{-1} further than deoxymyoglobin compared to the frequency for MbCO (taken at the same temperature). The core is defined as the distance between the four pyrrole nitrogen atoms; as this distance expands, the ν_2 line decreases in frequency. A semiquantitative relationship exists with the core expanding 0.002 Å/cm^{-1} (Spaulding et al., 1975). Although this cannot be directly used to measure iron−pyrrole nitrogen distances, especially in cases where the iron is displaced from the heme plane, it implies that the iron−pyrrole nitrogen distances of Mb*CO are longer than for MbCO and likely to be in the range of 2.03−2.05 Å (Jameson & Ibers, 1994). This is consistent with the EXAFS results presented here.

Second, ν_4, the oxidation state marker for Mb*CO, is shifted only 1 cm^{-1} from the deoxy value. The higher frequency for ligand-bound globins for this marker is related to depletion of the π antibonding orbitals. Thus, Mb*CO has little bonding (electronic) interaction with the CO ligand in the heme pocket. Third, the proximal histidine stretching frequency is shifted by 6 cm^{-1} to higher frequency relative to the value for deoxymyoglobin at the same temperature. Although this might argue for a stronger bond from iron to the proximal histidine nitrogen, such an interpretation requires no change in force constant, where in fact such a change is predicted due to increased tilt in going from Mb*CO to deoxymyoglobin (Rousseau & Friedman, 1988). Since Raman is extremely sensitive to structure, spin-state changes, and bonding, these data require a significant heme core expansion (and increases in iron−pyrrole nitrogen distances and iron displacement), significant change in charge density, and substantial relaxation of the iron relative to MbCO, with a final structure near that of deoxy-Mb. It should be added that the ability to observe the near-infrared band III and the proximal histidine stretching frequency for Mb*CO presumes a deoxy-like structure, since no similar near-infrared transition exists for MbCO and the resonance enhancement for the Fe−N_e stretch in MbCO is assumed to be small (e.g., the band has not been observed; Table 2).

On the basis of these data, we can assess to what extent the results of Table 1 meet these requirements and the possible reasons for the discrepancies. The earliest EXAFS results (Chance et al., 1983) have Fe−N_e and Fe−N_p distances that are identical within the error to the results seen here and are in agreement with the solution Raman data. The reported distance to the CO ligand (∼2 Å) is likely inconsistent with the infrared stretching frequency of the CO ligand (B state) for Mb*CO as well as the value of ν_4 in the resonance Raman. The presence of the ligand within van der Waals contact distance would be assumed to significantly perturb these vibrational frequencies. Figure 8 shows that a position for the CO ligand quite near the heme iron, as seen in Table 1, is not one of the better possible solutions; however, it is at a sharp local minimum. The EXAFS results of Teng et al. (1987) give Fe−N_p distances inconsistent with those reported here or with the solution Raman data. On the basis of our examination of their near-edge data, substantial photolysis was achieved and an intermediate was trapped that shows motion of the iron out of the heme plane. However, the EXAFS data show significant differences between the spectra of deoxy and Mb*CO. Since the sample was a concentrated MbCO film, the data were high in signal to noise; however, the dried film may have influenced the results. The EXAFS data of Powers et al. (1987) are

consistent with the results presented here in terms of the Fe−N_e and Fe−N_p distances. With respect to the position of the CO ligand, the results of Teng et al. and Powers et al. are consistent with the local minimum seen at ca. 2.5 Å from iron.

Table 1 also compares the results reported here to the two crystallographic results that are available. The Fe−N_e distance for the structure of Schlichting et al. (1994) is virtually identical to that provided by solution EXAFS. The Fe−N_p average distance is longer, based on the EXAFS results, and is quite consistent with the results suggested by examination of ν_2, the core-size marker. A minimum for the Fe−ligand (CO) distance is also seen by EXAFS, which is in agreement with the crystallographic results (which is also the best fit to the data). Overall, the differences are well within the respective errors of the two techniques. By contrast, the structural data provided by Moffat and co-workers (Teng et al., 1994) are inconsistent with the solution Raman, near-IR, and X-ray spectroscopy near-edge data that suggest an iron position with respect to the heme plane substantially displaced toward the proximal histidine side of the heme, almost to the deoxy value. This difference may be related to the functional properties conferred by the monoclinic space group of this crystal, or due to incomplete photolysis, with the structure based on an average of MbCO and Mb*CO conformations. In any case, even if the structural result is correct for the monoclinic crystal, it cannot be deemed relevant to the physiological solution state of the protein.

In conclusion, the crystallography results of Schlichting et al. (1994) are in complete agreement with the EXAFS results presented here within their respective errors. The greater precision of the EXAFS allows the bond lengths to be precisely defined, and these EXAFS results are consistent with Raman data collected previously. The crystallographic data allow discrimination between the multiple minima that would not be discernible by analysis of the EXAFS alone. An examination of the available spectroscopic data shows that the crystallographic results of Schlichting et al. are highly relevant to the physiological solution state and must be taken into account in any attempt to understand the incomplete relaxation process of the heme iron for the Mc*CO photoproduct at low temperature (Rousseau & Friedman, 1988). The structural data provided by Teng et al. (1994) are likely to be in error. The automated FEFF and crystallography approach that we outline here is likely to have a number of interesting future applications. The increased availability of crystal structures will provide accurate geometric models that can be further refined using EXAFS data. The ability to clearly visualize the possible solutions as provided by the AUTOFIT 1.0 suite of programs also gives an even-handed view of the structure and the error in bond distances.

REFERENCES

Alben, J. O., Beece, D., Browne, S. F., Doster, W., Eisenstein, L., Frauenfelder, H., Good, D., McDonald, J. D., Marden, M. C., Moh, P. P., Reinisch, L., Reynolds, A. H., Shyamsunder, E., & Yue, K. T. (1982) *Proc. Natl. Acad. Sci. U.S.A. 79*, 3744.

Ansari, A., Berendzen, J., Braunstein, D., Cowen, B. R., Fraunfelder, H., Hong, M. K., Iben, I. E. T., Johnson, J. B., Ormos, P., Sauke, T. B., Scholl, R., Schulte, A., Steinbach, P. J., Vittitow, J., & Young, R. D. (1987) *Biophys. Chem. 26*, 337.

Austin, R. H., Beeson, K., Eisenstein, L., Frauenfelder, H., & Gunsalus, I. C. (1975) *Biochemistry 14*, 5355.

Austin, R., Buhks, E., Chance, B., DeVault, D., Dutton, P. L., Frauenfelder, H., & Gol'danskii, V. I. (1987) *Protein Structure Molecular and Electronic Reactivity*, Springer Verlag, London.

Binstead, N., Strange, R. W., & Hasnain, S. S. (1992) *Biochemistry 31*, 12117.

Blackburn, N. J., Strange, R. W., Farooq, A., Haka, M. S., & Karlin, K. D. (1988) *J. Am. Chem. Soc. 110*, 4263.

Braunstein, D. P., Chu, K., Egeberg, K. D., Frauenfelder, H., Mourant, J. R., Nienhaus, G. U., Ormos, P., Sligar, S. G.; Springer, B. A., & Young, R. D. (1993) *Biophys. J. 65*, 2447.

Brown, W. E., Sutcliffe, J. W., & Pulsinelli, P. D. (1983) *Biochemistry 22*, 2914.

Brunger, A. T. (1987) *X-PLOR Version 3.1, A System for X-Ray Crystallography and NMR*, Yale University Press, New Haven, CT.

Caughey, W. S., Shimada, H., Choc, M. G., & Tucker, M. P. (1981) *Proc. Natl. Acad. Sci. U.S.A. 78*, 2903.

Chance, M. R. (1986) The proximal ligand in enzyme function, Ph.D. Thesis, University of Pennsylvania, Philadelphia, PA.

Chance, M. R. (1993) *Methods Enzymol. 226*, 97.

Chance, B., Fischetti, R., & Powers, L. (1983) *Biochemistry 22*, 3820.

Chance, M. R., Campbell, B. F., Hoover, R., & Friedman, J. M. (1987) *J. Biol. Chem. 262*, 6959.

Chance, M. R.; Courtney, S. H., Chavez, M. D., Ondrias, M. R., & Friedman, J. M. (1990) *Biochemistry 29*, 5537.

Chance, M. R., Sagi, I., Wirt, M. D., Frisbie, S. M., Scheuring, E. M., Chen, E., Bess, J. W., Henderson, L. E., Arthur, L. O., South, T. L., Perez-Alvarado, G., & Summers, M. F. (1992) *Proc. Natl. Acad. Sci. U.S.A. 89*, 10041.

Co, M. S., & Hodgson, K. O. (1981) *J. Am. Chem. Soc. 103*, 3200.

Cramer, S. P., Tench, O., Yocum, M., & George, G. N. (1988) *Nucl. Instrum. Methods A266*, 586.

Eaton, W. A., Hanson, L. K., Stephens, P. J., Sutherland, J. C., & Dunn, J. B. (1978) *J. Am. Chem. Soc. 100*, 4991.

Frauenfelder, H., & Wolynes, P. G. (1985) *Science 229*, 337.

Habenschuss, A., Ice, G. E., Sparks, C. J., & Neiser, R. A. (1988) *Nucl. Instrum. Methods*, 215.

Hasnain, S. S., & Strange, R. W. (1990) in *Biophysics & Synchrotron Radiation* (Hasnain, S. S., Ed.) p 104, Ellis Horwood Ltd., Chichester, U.K.

Iizuka, T., Yamamoto, H., Kotani, M., & Yoretani, T. (1974) *Biochim. Biophys. Acta 371*, 126.

Jameson, G. B., & Ibers, J. A. (1994) in *Bioinorganic Chemistry* (Bertini, I., Gray, H. B., Lippard, S. J., & Valentine, J. S., Eds.) Chapter 4, University Science Books, Mill Valley, CA.

Knowles, P. F., Strange, R. W., Blackburn, N. J., & Hasnain, S. S. (1989) *J. Am. Chem. Soc. 111*, 102.

Lee, P., Citrin, P., Eisenberger, P., & Kincaid, B. (1981) *Rev. Mod. Phys. 53*, 769.

Lim, M., Jackson, T. A., & Anfinrud, P. A. (1995) *Science 269*, 962.

Liu, H. I., Filipponi, A., Gavini, N., Burgess, B. K., Hedman, B., DiCicco, A., Natoli, C. R., & Hodgson, K. O. (1994) *J. Am. Chem. Soc. 116*, 2418.

Lytle, F. W., Sayers, D. E., & Stern, E. A. (1989) *Phys. B 158*, 701.

Makinen, M. W., & Churg, A. K. (1982) *Physical Bioinorganic Chemistry Series*, Part 1, Chapter 3, p 141,

Makinen, M. W., Houtchens, R. A., & Caughey, W. S. (1979) *Proc. Natl. Acad. Sci. U.S.A. 76*, 6042.

Marcolin, H. E., Reschke, R., & Trautwein, A. (1979) *Eur. J. Biochem. 96*, 119.

Miller, L. M., & Chance, M. R. (1994) *J. Am. Chem. Soc. 116*, 9662.

Miller, L. M., & Chance, M. R. (1995) *Biochemistry 34*, 10170.

Mustre de Leon, J., Rehr, J. J., Zabinsky, S. I., & Albers, R. C. (1991) *Phys. Rev. B44*, 4146.

Nordlander, E., Lee, S. C., Cen, W., Wu, Z. Y., Natoli, C. R., DiCicco, A., Filipponi, A., Hedman, B., Hodgson, K. O., & Holm, R. H. (1993) *J. Am. Chem. Soc. 115*, 5549.

O'Day, P. A., Rehr, J. J., Zabinsky, S. I., & Brown, G. E. (1994) *J. Am. Chem. Soc. 116*, 2938.

Powers, L., & Kincaid, B. M. (1989) *Biochemistry 28*, 4461.
Powers, L., Chance, B., Chance, M. R., Campbell, B., Friedman, J., Khalid, S., Kumar, C., Naqui, A., Reddy, K. S., & Zhou, Y. (1987) *Biochemistry 26*, 4785.
Quillin, M. L., Li, T., Olson, J. S., Phillips, G. N., Dou, Y., Ikeda-Saito, M., Regan, R., Carlson, M., Gibson, Q. H., Li, H., & Elber, R. (1995) *J. Mol. Biol. 245*, 416.
Ray, G. B., Li, X. Y., Ibers, J. A., Sessler, J. L., & Spiro, T. G. (1994) *J. Am. Chem. Soc. 116*, 162.
Rehr, J. J., & Albers, R. C. (1990) *Phys. Rev. B41*, 8139.
Rehr, J. J., Mustre de Leon, J., Zabinsky, S. I., & Albers, R. C. (1991) *J. Am. Chem. Soc. 113*, 5135.
Rehr, J. J., Zabinsky, S. I., & Albers, R. C. (1992) *Phys. Rev. Lett. 69*, 3397.
Roder, H., Berendzen, J., Bowne, S. F., Frauenfelder, H., Sauke, T. B., Shyamsundar, E., & Weissman, J. B. (1984) *Proc. Natl. Acad. Sci. U.S.A. 81*, 2359.
Rousseau, D. L., & Friedman, J. M. (1988) Transient and Cryogenic Studies of Photodissociated Hemoglobin and Myoglobin, in *Biological Applications of Raman Spectroscopy*, p 135, John Wiley and Sons, New York.
Rowlett, R. S., Chance, M. R., Wirt, M. D., Sidelinger, D. E., Royal, J. R., Woodroffe, M., Wang, Y. A., Saha, R. P., & Lam, M. G. (1994) *Biochemistry 33*, 13967.
Scheuring, E. M., Sagi, I., & Chance, M. R. (1994) *Biochemistry 33*, 6310.
Schlichting, I., Berendsen, J., Phillips, G. N., & Sweet, R. M. (1994) *Nature 371*, 808.
Sparks, C. J., Ice, G. E., Wong, J., & Batterman, B. W. (1982) *Nucl. Instrum. Methods 194*, 73.
Spartalian, K., Lang, G., & Yonetani, T. (1976) *Biochim. Biophys. Acta 428*, 281.
Spaulding, L. D., Chang, C. C., Yu, N. T., & Felton, R. H. (1975) *J. Am. Chem. Soc. 97*, 2517.
Spiro, T. G., & Burke, J. M. (1976) *J. Am. Chem. Soc. 98*, 5482.
Spiro, T. G., & Strekas, T. C. (1974) *J. Am. Chem. Soc. 96*, 340.
Spiro, T. G., Stong, J. D., & Stein, P. (1979) *J. Am. Chem. Soc. 101*, 2648.
Springer, B. A., Sligar, S. G., Olson, J. S., & Phillips, G. N. (1994) *Chem. Rev. 94*, 699.
Srajer, V., Schomacker, K. T., & Champion, P. M. (1986) *Phys. Rev. Lett. 57*, 1267.
Srajer, V., Reinisch, L., & Champion, P. M. (1988) *J. Am. Chem. Soc. 110*, 6656.
Stong, J. D., Burke, J. M., Daly, P., Wright, P., & Spiro, T. G. (1980) *J. Am. Chem. Soc. 102*, 5815.
Strange, R. W., Blackburn, N. J., Knowles, P. F., & Hasnain, S. S. (1987) *J. Am. Chem. Soc. 109*, 7157.
Teng, T. Y., Huang, H. W., & Olah, G. A. (1987) *Biochemistry 26*, 8066.
Teng, T. Y., Srajer, V., & Moffat, K. (1994) *Struct. Biol. 1*, 701.
Warburton, W. K. (1986) *Nucl. Instrum. Methods A246*, 541.
Westre, T. E., DiCicco, A., Filipponi, A., Natoli, C. R., Hedman, B., Solomon, E. I., & Hodgson, K. O. (1994) *J. Am. Chem. Soc. 116*, 6757.
Wittenberg, B. A., & Wittenberg, J. B. (1989) *Annu. Rev. Physiol. 51*, 857.
Zhu, L., Sage, J. T., Rigos, A. A., Morikis, D., & Champion, P. M. (1992) *J. Mol. Biol. 224*, 207.

BI9605503